

# Visualizing Macroscopic Inhomogeneities in Perovskite Solar Cells

Akash Dasgupta,<sup>II</sup> Suhas Mahesh,<sup>\*,II</sup> Pietro Caprioglio, Yen-Hung Lin, Karl-Augustin Zaininger, Robert D.J. Oliver, Philippe Holzhey, Suer Zhou, Melissa M. McCarthy, Joel A. Smith, Maximilian Frenzel, M. Greyson Christoforo, James M. Ball, Bernard Wenger, and Henry J. Snaith<sup>\*</sup>



Cite This: *ACS Energy Lett.* 2022, 7, 2311–2322



Read Online

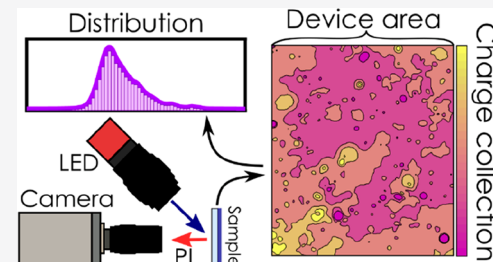
## ACCESS |

Metrics & More

Article Recommendations

Supporting Information

**ABSTRACT:** Despite the incredible progress made, the highest efficiency perovskite solar cells are still restricted to small areas ( $<1\text{ cm}^2$ ). In large part, this stems from a poor understanding of the widespread spatial heterogeneity in devices. Conventional techniques to assess heterogeneities can be time consuming, operate only at microscopic length scales, and demand specialized equipment. We overcome these limitations by using luminescence imaging to reveal large, millimeter-scale heterogeneities in the inferred electronic properties. We determine spatially resolved maps of “charge collection quality”, measured using the ratio of photoluminescence intensity at open and short circuit. We apply these methods to quantify the inhomogeneities introduced by a wide range of transport layers, thereby ranking them by suitability for upscaling. We reveal that top-contacting transport layers are the dominant source of heterogeneity in the multilayer material stack. We suggest that this methodology can be used to accelerate the development of highly efficient, large-area modules, especially through high-throughput experimentation.



Photovoltaic (PV) deployment at the multi-terawatt scale is of crucial importance in the quest to transition to a zero-carbon economy.<sup>1</sup> Since the power conversion efficiency (PCE) is one of the biggest determinants for the price of electricity per kilowatt-hour and therefore real-world adoption, developing highly efficient module-scale photovoltaics is a crucial avenue of research. While it took 60 years to engineer c-Si PV with a PCE of 26.7%,<sup>2</sup> it took hybrid perovskite PV only a decade to surpass 25.5%.<sup>2</sup> Apart from the inherent high-quality optoelectronic properties of hybrid perovskites, a key factor behind this rapid efficiency increase has been the broad suite of characterization methodologies developed by the semiconductor community, which reduce reliance upon trial and error experimentation. As instrumentation and our understanding of semiconductor processes advance, new characterization methods may emerge, offering powerful new ways to accelerate material discovery and optimization.

A fundamental principle, which has only become commonly exploited over the last 10 years, is that a good solar cell is also a good light-emitting diode.<sup>3,4</sup> This is because the trap states that capture excited charge carriers and reduce the amount of extractable work in a solar cell also facilitate recombination that does not emit photons. Thus, the photoluminescence quantum efficiency (PLQE) serves as an excellent proxy for the quality of photovoltaic materials or devices. Indeed,

luminescence measurements have emerged as a powerful “contactless probe” of loss mechanisms.<sup>5</sup> Since spontaneous emission is linked to physical quantities such as the carrier densities, the density of states, traps, and the quasi Fermi level splitting (QFLS), many internal properties and processes can be deduced from the luminescence.<sup>6</sup> This approach will only become more powerful as luminescence efficiencies improve and cells approach their thermodynamically limiting efficiencies.

While incredible advances have been made in PCEs, highly efficient perovskite solar cells are still restricted to small active areas ( $\leq 1\text{ cm}^2$ ). The simple nature of the processing techniques used for some emerging technologies such as metal halide perovskites introduces large local fluctuations at both short ( $<100\text{ nm}$ ) and long length scales ( $>10\text{ }\mu\text{m}$ ).<sup>7,8</sup> Even well-performing perovskite solar cells are seen to exhibit regions of both high and poor luminescence efficiencies. Understanding the origins of, and overcoming, these

Received: May 10, 2022

Accepted: June 8, 2022

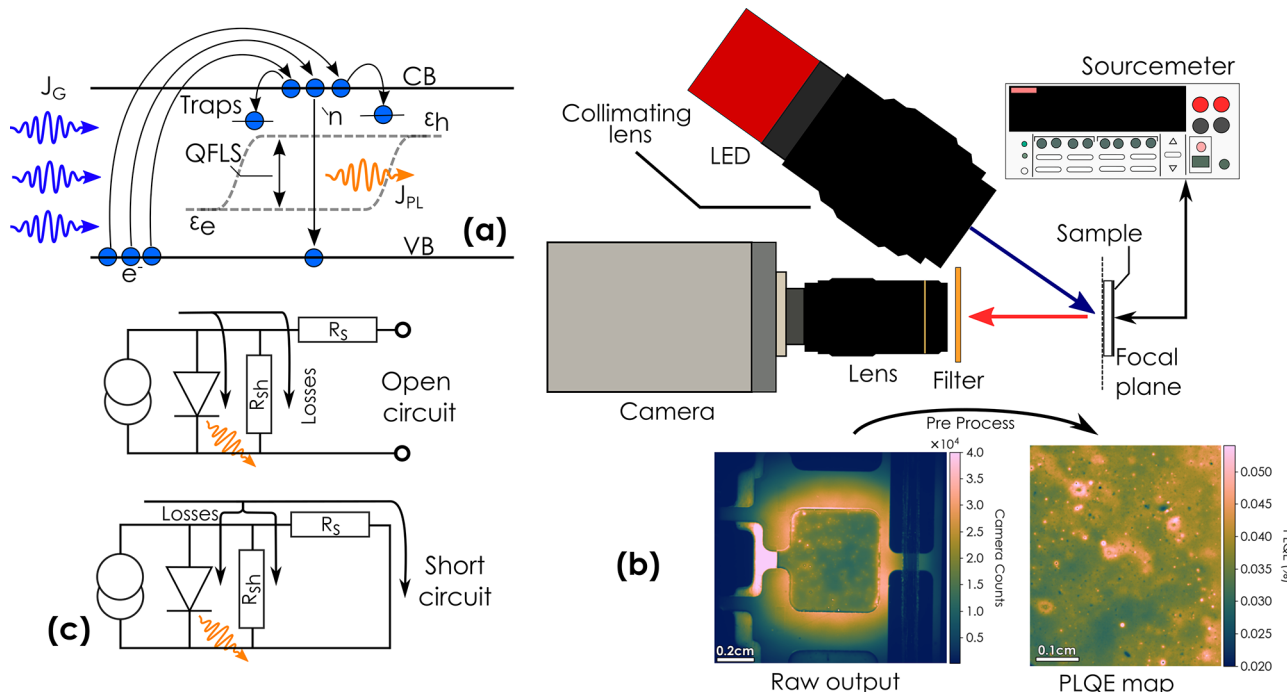


**Figure 1.** (a) Schematic of QFLS induced by optically excited carriers. Sub-band-gap states can mediate fast nonradiative recombination, which drains the bands of excited carriers. This changes the free-carrier concentration, which is also linked to the PLQE, making the PLQE an effective probe of both QFLS and charge carrier dynamics. (b) Schematic of luminescence imaging setup. Images are taken using an image sensor and lens, with a long-pass filter to block the 440 nm excitation light. The sample can be electrically biased using a source meter. A white diffuse reflector reference is used to calibrate the camera in order to determine the absolute luminescence and hence produce maps of the PLQE. (c) Equivalent circuit diagram for a simple solar cell at open and short circuit. PL occurs when current flows through the diode. PL at open circuit is reduced due to the shunt path, PL at short circuit may be affected by both.

heterogeneities is key to translating high-efficiency laboratory technology to wafer and full module scale manufacturing ( $\sim 250$  to  $20000\text{ cm}^2$ ).

A significant barrier to such upscaling is the lack of advanced characterization methods that can perform high-throughput measurements on an appropriate length scale. Maps of spatially resolved voltage loss have been constructed using hyperspectral luminescence imaging<sup>9</sup> and light-beam-induced current (LBIC) has been used in Si<sup>10</sup> and perovskites<sup>11</sup> to spatially map the short-circuit current. These techniques, however, can be time consuming (on the order of hours) and require access to specialized equipment.

Spatially resolved luminescence measurements provide a fast (approximately minutes) and relatively simple method for characterizing performance parameters and have been used in Si cells for a long time to identify series resistance hot spots in wafers.<sup>12–15</sup> In emerging PV materials such as perovskites, imaging of the PL over very small (nanometer to micrometer) length scales has produced maps of parameters such as QFLS.<sup>8,16</sup> Heterogeneities in luminescence on a device scale ( $>1\text{ mm}$ ) have also been measured, but many images of luminescence are presented in entirely arbitrary units, and comparisons with established mapping techniques or integrated measurements are necessary for a more robust analysis beyond simply identifying regions of low luminescence.<sup>16–19</sup> Indeed, a review of mapping techniques in perovskites<sup>20</sup> found that while luminescence measurements have been used effectively to map voltage losses on microscopic length scales, such maps are not well-established at macroscopic length scales.

Spatially resolved maps of parameters such as the ideality factor have been produced,<sup>21</sup> which can be used to understand the recombination mechanisms in a device. In terms of current loss, the optically measured parameter “current transport efficiency” ( $f_T$ ) introduced by Wong and Green<sup>22,23</sup> is a figure of merit.  $f_T$  was conceptualized for Si p–n junction cells, defined as the differential ratio of the extracted ( $\delta J$ ) current to the light-induced current ( $\delta J_L$ ), over an infinitesimally small voltage step, capturing losses in transporting the current from the p–n junction to the load at some voltage bias. Spatially resolved maps of  $f_T$  have been applied in Si<sup>24</sup> and later in perovskites. El-Hajje et al. measured spatially resolved maps of  $f_T$  in perovskite solar cells, across both a micrometer and millimeter length scale, evaluated near the open circuit.<sup>25</sup> Ren et al. measured similar maps near the maximum power point, for a range of intensities, and suggest that the differences in  $f_T$  observed in the samples of the study result from a difference in series resistance.<sup>26</sup> These maps of  $f_T$  provide a good way to probe the effects of factors such as series resistance at different voltage points. However, at short circuit, current loss is unlikely to be dominated by the effect of series resistance (see note 1 in the Supporting Information). Additionally,  $\delta J_L$  as defined in the formulation of  $f_T$  refers to the current which flows through the p–n junction. In the case of perovskite solar cells, this is likely to correspond to current which is extracted at the transport layers, and therefore losses in current due to charge carriers not reaching these layers, and remaining in the bulk, are not captured by this factor. The anomalous PL observed in many perovskite solar cells,<sup>27–29</sup> which has been linked to a loss in short-circuit current, is likely to have

contributions from carriers never reaching the charge extraction layers.

In this work, we introduce a relatively simple methodology by which we use a sensitive optical camera to image the luminescence of operational perovskite solar cells under varying optical irradiances and electrical biases. By applying the principle of detailed balance, we are able to derive spatial maps of many important optoelectronic and device parameters. We experimentally demonstrate that the ratio of short-circuit PLQE to open-circuit PLQE is an excellent measure of the effectiveness with which generated charge is collected in the case of perovskite solar cells and use this parameter to generate spatially resolved maps of current loss across centimeter-scale images. Furthermore, we show how spatially resolved maps of parameters, such as the QFLS and ideality factor, can be effectively used to reveal correlations between parameters by using a large amount of data extracted from measurements on a single sample. We also visualize the inhomogeneities introduced when seven widely employed charge transport layers (tin oxide nanoparticles ( $\text{SnO}_2$  NP),  $\text{C}_{60}$ , 2,2',7,7'-tetrakis[*N,N*-di(4-methoxyphenyl)amino]-9,9'-spirobifluorene (spiro-OMeTAD), nickel oxide ( $\text{NiO}_x$ ), poly[bis(4-phenyl)-(2,4,6-trimethylphenyl)amine] (PTAA), poly(*N,N'*-bis-4-butylphenyl-*N,N'*-bisphenyl)benzidine (poly-TPD), and [6,6]phenyl-C<sub>61</sub>-butyric acid methyl ester (PCBM)) are processed into a partial device stack, and we use quantitative metrics to describe this inhomogeneity. This can serve as a useful metric to rank materials and processing routes by suitability for upscaling. This is an important complement to the macroscopic quantification of the nonradiative recombination introduced by each layer—a technique already widely used by the community.

We combine luminescence measurements with detailed balance calculations to create maps of the following parameters which link directly to PV performance losses: QFLS at open circuit, which is closely linked to  $V_{\text{OC}}$  loss; charge collection quality, a metric linked to  $J_{\text{SC}}$  loss; and the ideality factor  $n$ , which encodes information about the dominant recombination mechanism in the material. The QFLS and ideality factor maps are produced in this work using adaptations of methods previously reported.<sup>30–33</sup> The luminescence-derived charge collection quality as a metric for short circuit current loss will be justified and experimentally validated in a later section.

When charge carriers are optically excited in a solar cell, the chemical potentials of electrons and holes become nonidentical (“quasi Fermi levels”). The difference between these two quasi Fermi levels (“quasi Fermi level splitting”) is equal to  $eV_{\text{OC}}$  in an ideal device, where  $e$  is the elementary charge (Figure 1a). However, a misalignment of energy levels at the interfaces or lack of selectivity of the charge extraction heterojunctions often causes  $eV_{\text{OC}}$  to be lower than the internal QFLS.<sup>30,34</sup>

The principle of optoelectronic reciprocity<sup>4,32,35</sup> allows us to link the internal QFLS to the photoluminescence quantum efficiency (PLQE):

$$\text{QFLS} = \text{QFLS}_{\text{rad}} + kT \ln \text{PLQE} \quad (1)$$

where  $\text{QFLS}_{\text{rad}}$  is the QFLS in the radiative limit, which can be calculated from the active material’s absorption spectrum,<sup>32,36</sup> and  $k$  is the Boltzmann constant. A more thorough derivation of eq 1 is given in note 2 in the Supporting Information. A schematic of this process is shown in Figure 1a. A spatially resolved map of the PLQE therefore allows us to reconstruct a map of the QFLS. This is a contactless measurement and so

can be done for “half-stacks” (partially constructed solar cells) as well as full devices.

The nature of the dominant charge recombination mechanism in the device can be inferred from the ideality factor ( $n$ ). The ideality factor is featured in the classical diode equation

$$J_{\text{D}} = J_0(e^{eV_{\text{D}}/nkT} - 1) \quad (2)$$

where  $J_{\text{D}}$  and  $V_{\text{D}}$  are the diode current density and voltage, respectively,  $J_0$  is the diode saturation current density, and  $T$  is the temperature of the cell. The ideality factor, which is unity in an ideal cell, was traditionally understood to tend toward 2 with increasing first-order nonradiative recombination, understood through the Shockley–Read–Hall model.<sup>37,38</sup> However, recent reports<sup>31,39</sup> have provided greater clarity by distinguishing between the influence of bulk and interfacial recombination (occurring at the perovskite/transport layer interfaces) on the ideality factor.

The ideality factor may be found optically using a method applied by Sarritzu,<sup>32</sup> with the relation

$$\ln(I_{\text{suns}}) + C = \frac{\text{QFLS}}{nkT} \quad (3)$$

Here,  $I_{\text{suns}}$  is the illumination irradiance expressed as number of suns (1 sun is AM1.5 100 mW cm<sup>-2</sup> equivalent irradiance for that band gap) and  $C$  is a constant term. A more thorough derivation of eq 3 is also given in note 2 in the Supporting Information. Thus, the ideality factor for each point on the active area can be calculated using intensity-dependent QFLS maps. The distribution of  $n$  vs QFLS therefore gives us information about the dominant type of recombination.

For our imaging setup (Figure 1b) we used a sensitive Si CMOS camera (Andor Zyla 4.2, Oxford Instruments),<sup>40</sup> which is suitable for low-intensity acquisitions. Samples can be imaged under both controlled optical excitation (440 nm LED; 0–1 sun equivalent photon flux) and electrical bias. In the case of full devices, we used the test device itself to calibrate the optical intensity in terms of number of suns by comparing the short-circuit current to the short-circuit current measured on a well-calibrated solar simulator. A long-pass filter is used in the imaging set up to block the 440 nm excitation light from reaching the camera.

The number of counts recorded by each camera pixel scales linearly with the number of photons emitted by the associated point on the sample, assuming that the signal is significantly larger than the noise floor. The sample is aligned to be in the focal plane of the lens and coincides with the center of the illumination, where the illumination profile has the flattest intensity profile (see Figure S3).

When the PLQE is desired, a high-reflectance  $\text{BaSO}_4$  plate is imaged, without filtering, as a reference. A more detailed description, including correction factors used, can be found in note 3 in the Supporting Information.

Before undertaking this work, we were not certain what features and inhomogeneities would exist at the 0.01–1 mm length scale that our imaging setup resolves. In order to verify the general validity of our approach, we recorded luminescence images on a selection of different perovskite solar cells. We imaged a well-performing  $\text{FA}_{0.83}\text{Cs}_{0.17}\text{Pb}(\text{I}_{0.83}\text{Br}_{0.17})_3$  device (18.5% PCE, 1.6 eV band gap; see Figure S5 and Table S3 in the Supporting Information) and characterized the current–voltage response in four different ways (Figure 2a): two

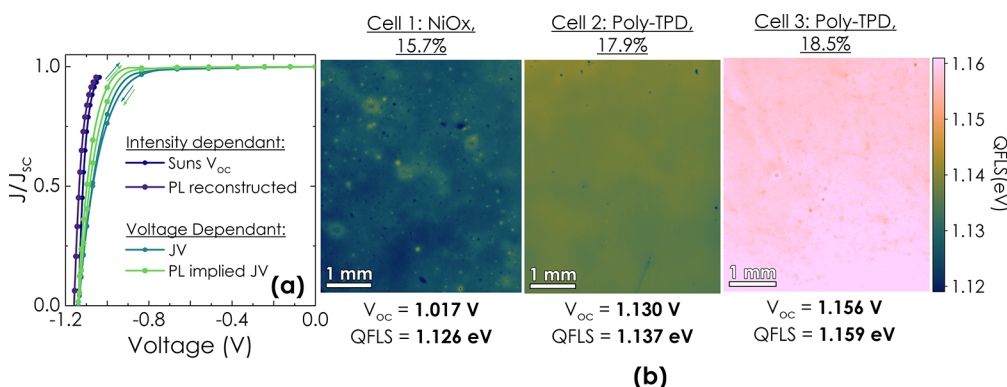


**Figure 2.** Reconstructed JV curves and QFLS maps measured under 1 sun illumination. (a) Current–voltage response of a 1.6 eV band gap  $\text{FA}_{0.83}\text{Cs}_{0.17}\text{Pb}(\text{I}_{0.83}\text{Br}_{0.17})_3$  perovskite solar cell measured in four different ways. The suns– $V_{OC}$  curve was constructed by measuring the  $V_{OC}$  value across a range of illumination intensities. The “PL reconstructed” curve (optical version of suns– $V_{OC}$ ) was constructed from the QFLS at open circuit measured at different illumination intensities. The “PL implied JV” was constructed using the method described by Stolterfoht et al.,<sup>27</sup> which links PL intensity at different voltages to the extracted current. The arrows indicate the direction of the scan. (b) QFLS maps from 1.6 eV band gap Formamidinium-Caesium (FA-Cs) mixed halide perovskite solar cells, with  $\text{NiO}_x$  (cell 1) and poly-TPD (cells 2 and 3) as HTLs. All use a PCBM/BCP/Au top contact. Power conversion efficiencies of the samples are indicated (%).

electrical measurements under illumination and two optical measurements analogous to the electrical measurements. The two electrical measurements include (1) measuring the current while sweeping the voltage (labeled “JV”) and (2) measuring the  $V_{OC}$  value while sweeping the intensity, which is used to infer the current density (also known as the suns– $V_{OC}$  method<sup>41</sup>). The corresponding optical measurements include (1) inferring the current density from the PL intensity averaged across the device as the voltage was swept (drawing upon the approach of Stolterfoht et al.,<sup>27</sup> labeled “PL implied JV”) and (2) inferring voltage from the average PLQE at open circuit while the illumination intensity is changed (using eq 1 and taking the QFLS to be the voltage; labeled “PL reconstructed”).

The curves measured by all four methods vary, as would be expected from macroscopic measurements of the same properties. Furthermore, the electrically measured curves show excellent agreement with the curves derived from averaging the PL images (Figure 2a). The fill factor appears to be enhanced in the suns– $V_{OC}$  and PL-reconstructed curves, as these measurements were performed at open circuit, where the series resistance has no influence. This validates our setup’s ability to measure absolute PL intensities and reconstruct the QFLS across a range of bias conditions.

To further validate the setup and assess the types of inhomogeneities present in full devices, we reconstructed QFLS maps at 1 sun illumination for 1.6 eV band gap cells of two different architectures (Figure 2b): cell 1,  $\text{NiO}_x$ /perovskite/PCBM; cells 2 and 3, poly-TPD/perovskite/PCBM.

In all of the captured PL images, we observe a number of spatial inhomogeneities at the millimeter length scale, with the better-performing poly-TPD cells exhibiting a more homogeneous QFLS distribution in comparison to the  $\text{NiO}_x$  cell. In a later section, we present a fuller analysis of the heterogeneity introduced by all of the widely used transport layers. On comparing the two poly-TPD cells, we can see that, despite identical processing conditions, the variability is still quite different. This is a common feature of devices processed by simple methods such as spin-coating and is likely to be a significant barrier to scale-up.

The poorly performing  $\text{NiO}_x$ -based cell also has a larger difference between the mean QFLS and that measured, indicating an energy level misalignment at a heterojunction or a lack of charge selectivity.<sup>30,34</sup> Notwithstanding this small difference, the average values of the QFLS are still close to the measured  $V_{OC}$  value, and they agree very well for both of the poly-TPD-based cells, once again validating our ability to correctly reproduce QFLS maps.

Furthermore, though the luminescence is rather inhomogeneous in the  $\text{NiO}_x$ -based cell, there are localized regions on the map that approach the luminescence efficiencies of the well-performing poly-TPD-based cells. Their existence indicates that an intrinsic limitation of the material is not at work here: with an optimization of the processing conditions, we can expect to fabricate a device with uniformly bright luminescence. We suggest that such luminescence imaging could be combined with deposition equipment so that the performance can continuously be monitored *in situ*, accelerating device optimization. With an increase of laboratory automation, we can also envision that such luminescence images will be fed to active learning models that can vary processing parameters until the luminescence is maximized.

While the protocol for making spatial maps of quasi Fermi level splitting (and hence voltage losses) from luminescence measurements is well-established, a method for estimating the total current loss at short circuit in a spatially resolved fashion has not been successfully applied to perovskites. Here we utilize and experimentally verify an expression that links the current loss to luminescence at short circuit, enabling us to visualize regions of current loss over a cell’s active area.

An ideal solar cell at short-circuit (SC) collects all the generated carriers and therefore will not emit any photons. In practice, however, perovskite solar cells have been observed to emit significant PL even at short circuit.<sup>27</sup> Furthermore, a transient increase in PL at short circuit has been observed for some cell types, in conjunction with a transient increase in current loss,<sup>28</sup> and it has been suggested that the ratio of PL at SC to open-circuit (OC) may be linked to the charge extraction efficiency.<sup>29</sup> Similar observations in silicon PV cells have been attributed to diffusion-limited carriers generated in the bulk that were unable to reach the p–n junction,<sup>9,10</sup> and in some instances the ratio of PL at OC and SC has been used to

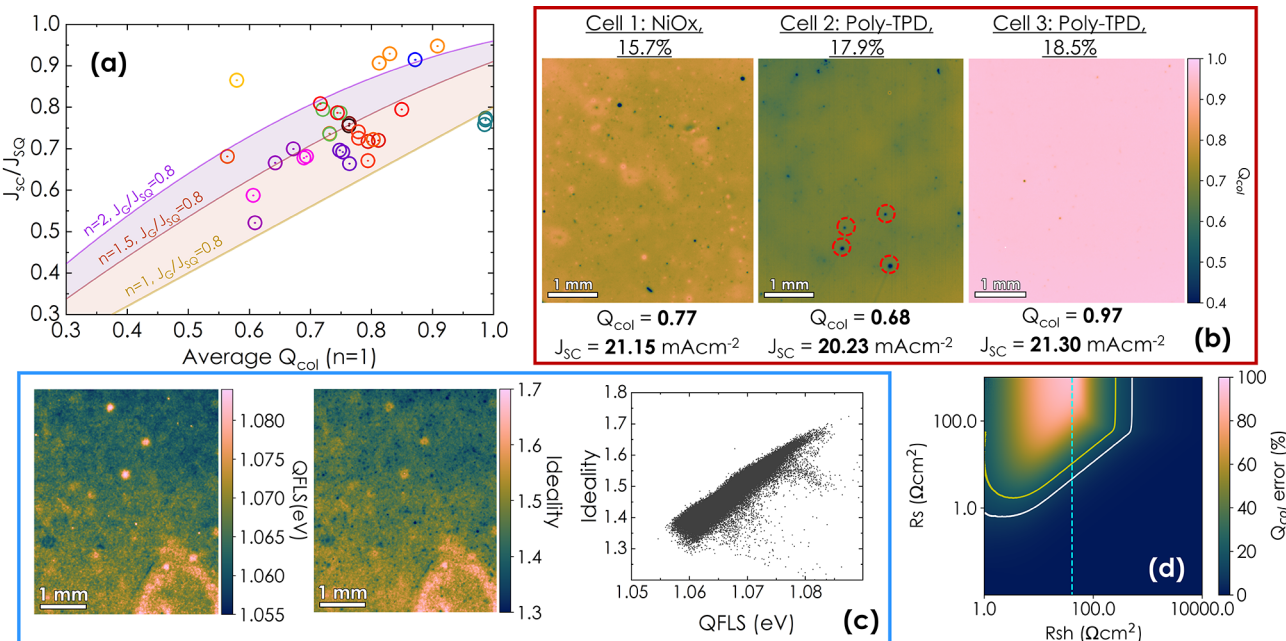


**Figure 3.** (a) Normalized  $J_{SC}$  of different perovskite solar cells vs charge collection quality (averaged across cell area, assuming unity ideality factor).  $J_{SC}$  has been normalized to the Shockley–Queisser (SQ) current density, to account for the different band gaps of cells. Lines drawn indicate the predicted normalized  $J_{SC}$  from the measured  $Q_{col}(n=1)$  from eq 11 for ‘true’ values of  $n = 1, 1.5, 2$  (assuming the generation current density is 80% of the SQ limit maximum current density). Cells from the same substrate are given the same color (details are given in the Supporting Information). All measurements were taken at 1 sun equivalent photon flux, and cells were illuminated for 30 s before measurement to bring the device to a steady state. (b) Collection quality map of the cells shown in Figure 2. Areas of particularly poor collection quality are highlighted with red circles. Ideality factor maps were incorporated in these measurements. Power conversion efficiencies of the samples are indicated (%). (c) (left to right) Map of QFLS, map of ideality factor, and scatter plot of ideality factor vs QFLS, where each data point is taken from a spatial point from the two maps on the left. (d) Error in the  $Q_{col}$  value ( $Q_{col} - J_{SC}/J_G$ ) as a percentage of  $Q_{col}$  from simulation. White and yellow lines show boundaries of 10% and 15% error, respectively. The blue line is the point where, for lower shunt resistances, the ratio of current through the shunt  $V_s$  through the diode exceeded 1000; for  $R_{sh}$  under the blue line, the PL is under the sensor detector limit.

estimate diffusion lengths in silicon samples.<sup>42</sup> In perovskite devices, one possible explanation for the residual PL at SC could be the screening of the internal field due to ion redistribution, leaving the absorber with a zero net field, where the charge can undergo internal recombination before being transported out of the device.<sup>28</sup> Alternatively, perovskite films, due to processing inhomogeneities, may contain regions of isolated material not properly contacted with the electrodes.

Rau links this same anomalous “residual luminescence” observed at short circuit in Cu(In,Ga)Se<sub>2</sub> solar cells directly to the ratio of the short-circuit current to the current generated in the material.<sup>43</sup> In the case of perovskite solar cells, we verify that a similar expression does in fact correlate with losses in short-circuit current and use it to generate spatially resolved maps of “current collection” at short circuit.

We can understand the estimation of current loss intuitively from a comparison between the luminescence intensities from the PV cell at short circuit and open circuit. At open circuit, every generated e–h pair has three possible fates: recombine radiatively, recombine nonradiatively, or flow through the shunt resistance from the equivalent circuit model (Figure 1c). Luminescence can originate only from charge carriers that flow through the diode in the equivalent circuit model.

The extracted current density from the cell ( $J$ ) is linked to the luminescence through the ideality factor, a “fudge-factor” introduced into the diode equation to account for the mixture of recombination mechanisms that operate in a cell. On comparison of the radiative recombination current density

( $J_{rad}$ ) to the total current density  $J$ , the PL intensity at open circuit can be shown to be proportional to the generation current density ( $J_G$ ) to the power of  $n$ , where  $n$  is the ideality factor

$$J = J_G - J_0 e^{QFLS/nkT} \quad J_{rad} = J_0 \cdot EQE_{EL}(V) \cdot e^{QFLS/kT} \quad (4)$$

$$\text{at OC: } J = 0 \Rightarrow J_G = J_0 e^{QFLS_{OC}/nkT} \quad (5)$$

$$\Rightarrow J_{rad,OC} = J_0^{1-n} \cdot EQE_{EL}(V) \cdot (J_G)^n \quad (6)$$

since at open circuit, all generated carriers must recombine.

At short circuit, the majority of photogenerated charge-carriers are extracted as load current, quenching the PL. Some carriers are not extracted as load current and instead flow through a shunt pathway or recombine in the perovskite bulk. The current density that is not extracted at short circuit,  $J_G - J_{SC}$  is responsible for the anomalous PL at SC:

$$\text{at SC: } J = J_{SC} \Rightarrow J_G - J_{SC} = J_0 e^{QFLS_{SC}/nkT} \quad (7)$$

$$\Rightarrow J_{rad,SC} = J_0^{1-n} \cdot EQE_{EL}(V) \cdot (J_G - J_{SC})^n \quad (8)$$

Rearranging eqs 6 and 8, we get:

$$J_G - J_{SC} = (J_0^{1-n} \cdot EQE_{EL}(V) \cdot J_{rad,SC})^{1/n} \quad (9)$$

$$J_G = (J_0^{1-n} \cdot EQE_{EL}(V) \cdot J_{rad,OC})^{1/n} \quad (10)$$

Assuming that the ideality factor and  $\text{EQE}_{\text{EL}}(V)$  does not change between OC and SC, we can write

$$Q_{\text{col}} = \frac{J_{\text{SC}}}{J_G} = 1 - \left( \frac{J_{\text{rad},\text{SC}}}{J_{\text{rad},\text{OC}}} \right)^{1/n} = 1 - \left( \frac{\text{PLQE}(\text{SC})}{\text{PLQE}(\text{OC})} \right)^{1/n} \quad (11)$$

where  $Q_{\text{col}}$  is a parameter we dub the “charge collection quality”. In a device with zero series and infinite shunt resistance,  $Q_{\text{col}}$  would be identical to the internal quantum efficiency. While  $Q_{\text{col}}$  is a function of the ideality factor, it remains much faster to measure PLQE(SC) and PLQE(OC) in comparison to the ideality factor, which requires a full intensity-dependent measurement and fitting of the slope of the QFLS as a function of intensity for every pixel in the map. If a fast measurement is required, one can measure only the PLQE(SC) and PLQE(OC) values and assume an ideality factor of unity, or any other value that corresponds to the macroscopically averaged ideality factor of the cell, to get an approximate value of  $Q_{\text{col}}$ , which still correlates with the current loss (See note 5 in the Supporting Information for full justification).

When the effects of shunt and series resistances are included,  $Q_{\text{col}}$  can underestimate or overestimate the internal quantum efficiency. Nevertheless, as we shall experimentally demonstrate, it remains a useful metric, as it is found to correlate with current loss.

To experimentally verify the validity of the expression for  $Q_{\text{col}}$  (eq 11), we measured  $Q_{\text{col}}(n=1)$  for a large number of cells, in both positive–intrinsic–negative (p–i–n) and n–i–p architectures, with band gaps varying from 1.6 to 1.8 eV, with a variety of different hole-transporting layers (HTLs) and electron-transporting layers (ETLs) (see the Supporting Information for details). For these measurements the ideality factor was considered to be unity, as described. By measuring the average PL intensity over the active area at open circuit and short circuit, we can calculate an average  $Q_{\text{col}}(n=1)$  for the device (eq 11). The relationship between  $J_{\text{SC}}/J_G$  and  $Q_{\text{col}}(n=1)$  can be calculated for different “true” values of ideality factor and accounting for a reasonable loss in current due to reflection losses and parasitic absorption. If the electrically measured  $J_{\text{SC}}$  is shown to follow this relation with  $Q_{\text{col}}(n=1)$ , the validity of the expression (eq 11) is confirmed. To minimize the impact of shunt and series resistance on  $Q_{\text{col}}$ , only “good” devices were chosen, meaning that the average shunt resistance may be considered to be much greater than the solar cell’s output resistance  $\frac{V_{\text{OC}}}{I_{\text{SC}}}$ .

Measurements were made under an equivalent irradiance of 1 sun for each cell, with a preillumination of 30 s under open-circuit conditions to ensure the device was at a steady state. In Figure 3a, we show a plot of the band-gap-normalized  $J_{\text{SC}}$  (taken to be the Shockley–Queisser (SQ) current density) versus the spatially averaged charge collection quality  $Q_{\text{col},n=1}$ . The values of  $Q_{\text{col},n=1}$  vs  $\frac{J_{\text{SC}}}{J_{\text{SQ}}}$  fall within a range of values

predicted by eq 11, for ideality factors ranging from 1 to 2 and assumption of an average 20% loss in the generation current density from the SQ limit (typical for cells produced in our laboratories). This confirms the qualitative validity of our expression for  $Q_{\text{col}}$ . Apart from the variation in ideality factor, we may attribute some of the spread in data to some additional

factors: namely, the variation of series and shunt resistances and limitation of setting the intensity to exactly 1 sun.

We now briefly comment on the impact of series and shunt resistances on  $Q_{\text{col}}$ . Luminescence originates from radiative recombination in the semiconductor bulk, which in the equivalent circuit model is a certain fraction of the current flowing through the diode. If a fraction of the current is able to flow through a different pathway, namely the series or shunt resistor, then the luminescence will be altered. At open circuit, shunt pathways divert charge away from the perovskite bulk (equivalently more current flows through the shunt resistor as opposed to the diode), diminishing luminescence. The series resistance has no influence at open circuit. At short circuit, the presence of a series resistance results in a nonzero potential difference across the parallel shunt and diode components, hence causing some current to flow through the diode, resulting in luminescence at short circuit, with increasing series resistance. However, even at short circuit some current will flow through the shunt pathways, causing the luminescence to diminish, which does not correspond to the collected current. Using the equivalent circuit model, we can calculate how the internal quantum efficiency  $\frac{J_{\text{SC}}}{J_G}$  varies with values of  $R_S$  and  $R_{\text{SH}}$

and compare this to the estimated  $Q_{\text{col}}$  value (assuming the absolute PL is proportional to current flowing through the diode). Through this, we can estimate the error in  $Q_{\text{col}}$  introduced by  $R_S$  and  $R_{\text{SH}}$ . We show that the values for the internal quantum efficiency and  $Q_{\text{col}}$  agree with each other very closely (<10% error), apart from the conditions when the shunt resistance is very low and where the series resistance is very high (Figure 3d; see note 4 in the Supporting Information for full details). In this case, we found that  $Q_{\text{col}}$  tends to overestimate  $\frac{J_{\text{SC}}}{J_G}$ , but this only occurs in extreme cases.

We now comment on the spatial inhomogeneity in  $Q_{\text{col}}$  observed in the three cells we present in Figure 3a. Since the presence of traps influence the device performance on many fronts, it is important to answer the following question: does a poor  $Q_{\text{col}}$  imply a poor QFLS, both being mediated by traps? If so,  $Q_{\text{col}}$  maps would be unnecessary, since QFLS maps essentially provide the same information. Looking at the QFLS and  $Q_{\text{col}}$  maps of cell 2 (Figures 2b and 3b), we can see very clearly that this is not the case—regions of poor  $Q_{\text{col}}$  are not always detectable on QFLS maps. The red circles in Figure 3b highlight areas where the values of  $Q_{\text{col}}$  (and hence the current) are particularly low. These features are completely unobservable with the QFLS map (Figure 2b). Could these low-luminescence regions instead be explained by shunts? The absence of these features in the map taken at OC (Figure 2b) shows that they are not shunts, for shunting effects are active at both OC and SC.

The maps presented (Figures 2b and 3b) indicate that the average value and the inhomogeneity in QFLS (a proxy for  $V_{\text{OC}}$ ) and  $Q_{\text{col}}$  (a proxy for  $J_{\text{SC}}$ ) can vary independently in devices, making the characterization of both essential for a full understanding of spatially resolved losses. To illustrate—while cell 2 (poly-TPD-based) has superior QFLS in comparison to cell 1 ( $\text{NiO}_x$ -based), it has a lower average  $Q_{\text{col}}$  value (Figure 3b). Furthermore, the two have similar levels of inhomogeneity in  $Q_{\text{col}}$ , despite cell 2 having a far more homogeneous QFLS map. To reiterate, QFLS and  $Q_{\text{col}}$  can vary independently, and both are required to fully map loss mechanisms.

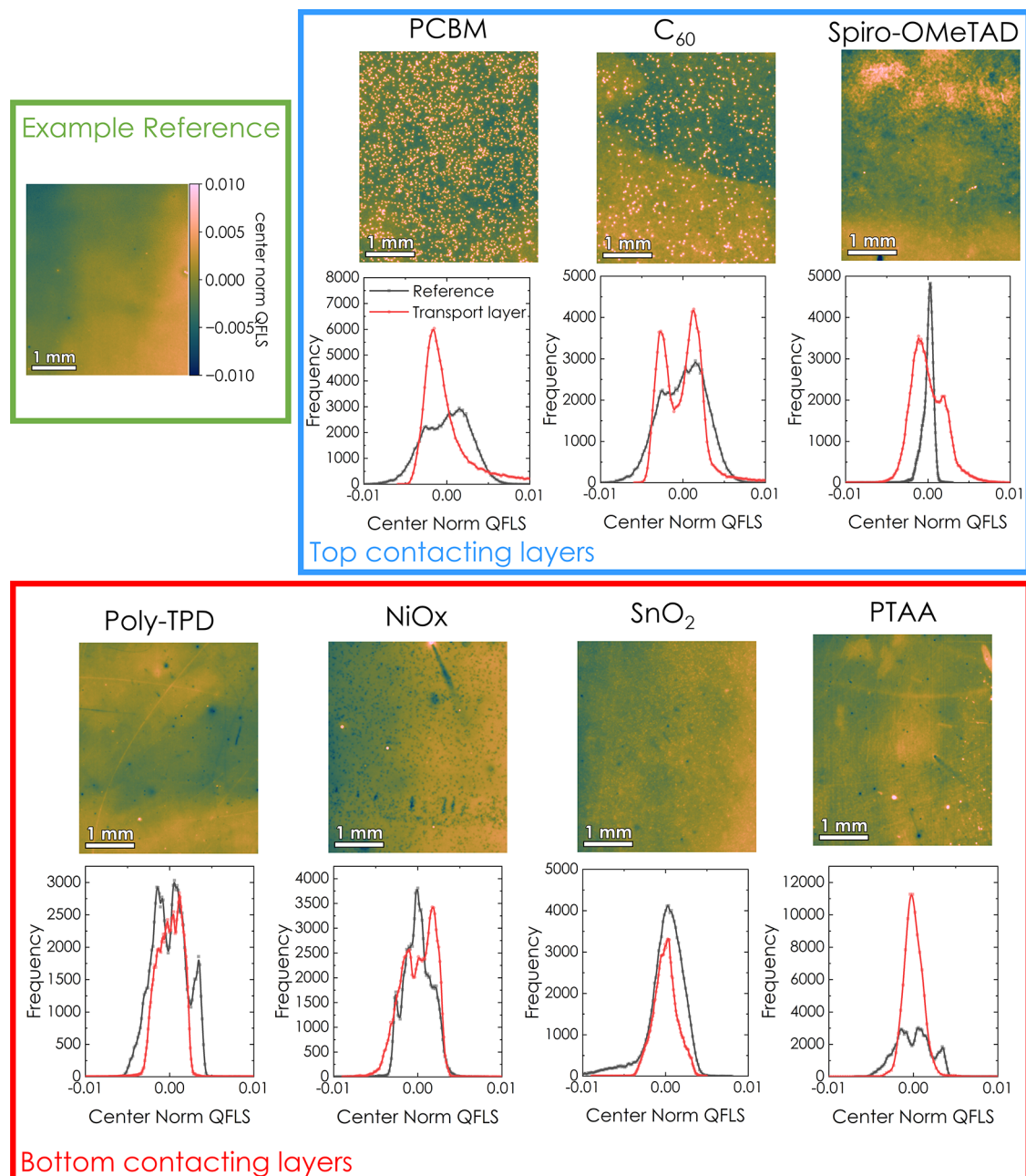


**Figure 4.** Center-normalized QFLS maps (top, same scale as Example Reference) and histograms of the same maps (bottom) for different transport layer half-stacks. Different perovskite blends were used for the samples; thus, the distribution of a neat perovskite film on glass for each sample is shown on the histograms and an example reference is shown. The same illumination (1 sun for a 1.6 eV cell) was used for all the samples for consistency, and the color scale bar is the same for all images (as shown in the example reference).

Metrics such as  $Q_{\text{col}}$  acquire special significance in the context of in-line metrology and high-throughput experimentation. A significant advantage of this approach for identifying inhomogeneities in current loss is that each device measurement requires only a few minutes, in comparison to several hours for an equivalent LBIC mapping approach.

In addition to maps of QFLS and  $Q_{\text{col}}$ , we can study directly maps of the ideality factor, which provide information about the recombination processes at work in a solar cell. Plotting the ideality factor vs QFLS for each pixel in the device reveals that more luminescent pixels have higher ideality factors. This trend is evidence that the performance of the cell under measurement is limited by interfacial recombination, not bulk

recombination. This validates a recent study<sup>31</sup> which suggests that, in devices dominated by interfacial recombination, the ideality factor will, rather counterintuitively, increase with increasing QFLS.

Thus, the natural spatial variation in a solar cell enables us to demonstrate this trend with a large amount of data acquired from only a single device, in a timespan of minutes. The ability to capture such large amounts of data opens up the possibility of exploring previously unknown relationships between various semiconductor and device properties. There is an exciting scope for the application of novel statistical techniques and machine learning methods to analyze such data sets.

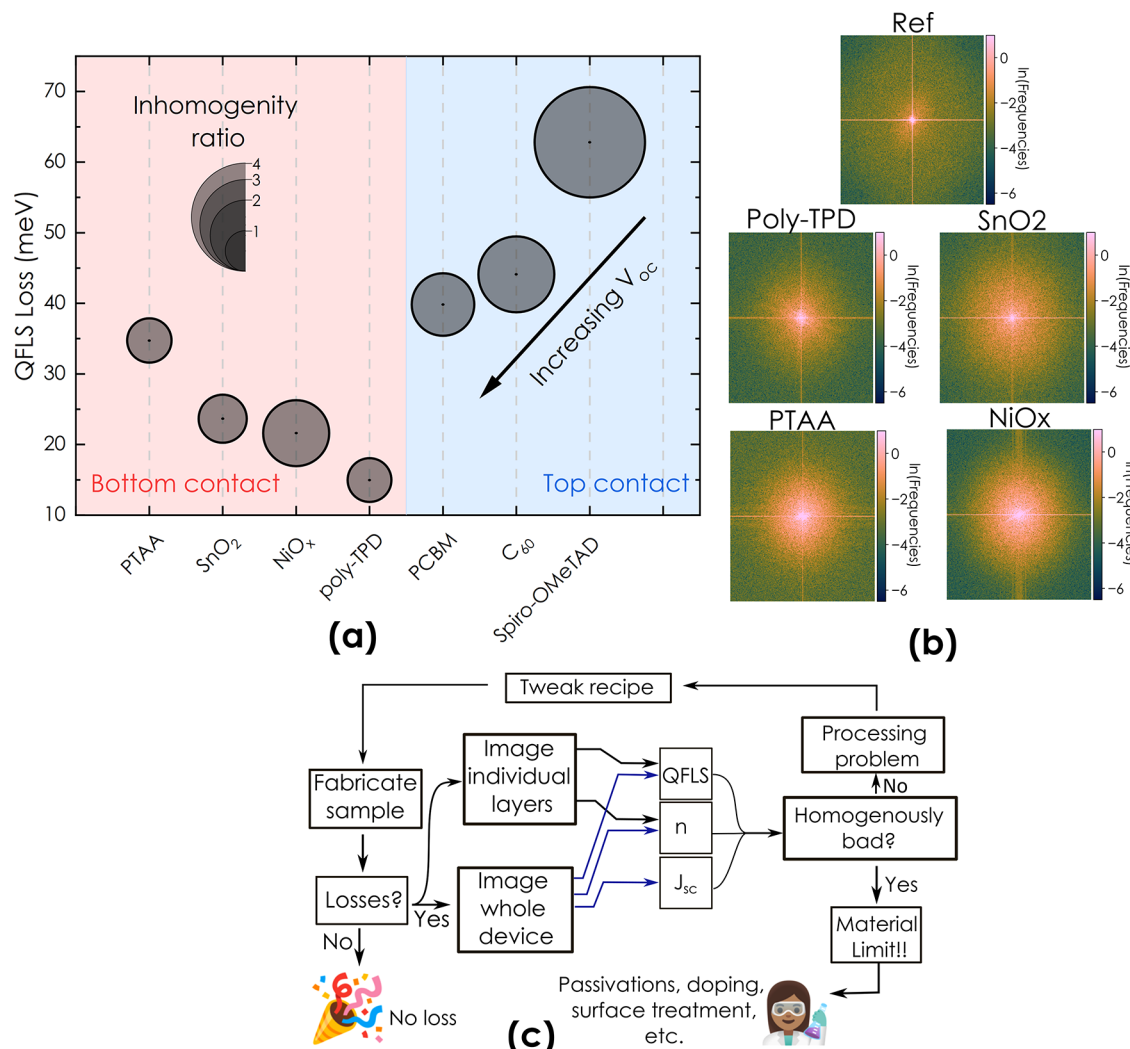


**Figure 5.** Comparison of the inhomogeneity induced by the different transport layers shown in Figure 4. (a) Plot of QFLS loss and inhomogeneity ratio for the different transport layers shown in Figure 4. The area of the bubbles is proportional to the inhomogeneity of the transport layer (with respect to a reference of the corresponding perovskite on glass). (b) Fourier transforms of the center-normalized QFLS maps from Figure 4. The reference shows a strong cross-hair pattern typical of a smooth real profile, while all of the TLs show some higher frequency terms and the superposition of a Gaussian-like profile. (c) Schematic of proposed optimization workflow for identifying and addressing inhomogeneities in a device, using the luminescence measurement setup.

*A priori*, the source of this significant inhomogeneity at the 0.1–1 mm scale is unclear. It could be rooted in certain layers or interfaces or be the result of certain processing methods. Such sources of heterogeneity can be characterized by acquiring luminescence maps at each step of solar cell fabrication and quantifying each step's effect on heterogeneity.

We reconstructed QFLS maps for a wide variety of partially fabricated cells, quantitatively measuring the heterogeneity introduced at each stage of device fabrication. Our study includes seven widely used transport layers (TL), PCBM, C<sub>60</sub>, spiro-OMeTAD, poly-TPD, NiO<sub>x</sub>, SnO<sub>2</sub>, and PTAA, coated upon or beneath perovskite thin films as “half-stacks”.

A glass\transparent conductive oxide (TCO)\TL\perovskite stack was used for “bottom contacting” transport layers, and a glass\perovskite\TL stack was used for top contacting layers. For details about the perovskite compositions and fabrication procedures used, see **Sample fabrication** in the Supporting Information. In order to quantify the additional inhomogeneity introduced by a transport layer in contact with these different

perovskite films, a reference sample of neat perovskite was deposited on glass in each case.

Luminescence maps of different samples cannot be directly compared for heterogeneity, as the mean value of the QFLS will be different for different samples. Therefore, a normalized measure of spread is needed. The statistical distribution of luminescence data obtained could have a spread that is a function of the mean (for example, in a Poisson distribution the standard deviation is proportional to the root of the mean). In order to compare between different samples, we define the center normalized QFLS:

$$\text{center norm QFLS}_{i,j} = \frac{\text{QFLS}_{i,j} - \langle \text{QFLS} \rangle}{\langle \text{QFLS} \rangle} \quad (12)$$

where *i* and *j* are indices of points on the QFLS map, and  $\langle \text{QFLS} \rangle$  is the mean QFLS of the sample. The center-normalized QFLS will be centered on 0 and is normalized by the mean, making distributions between different samples comparable.

Maps of center-normalized QFLS are shown in Figure 4, along with the corresponding binned distributions with respect to the neat perovskite reference film. We can observe, in general, that each transport layer introduces visibly significant heterogeneity to the neat perovskite on the millimeter length scale.

The PCBM sample and to a lesser extent the C<sub>60</sub> sample exhibit a large population of bright emissive spots (high QFLS) across their surfaces. Consequently, the PCBM histogram has a heavy right tail. We interpret these bright speckles to be regions where the fullerene is either not directly electronically contacting or not present (i.e., pinholes) on top of the perovskite film. In line with the superior homogeneity of C<sub>60</sub> that we visualize, it is often used as an interlayer alongside an ETL to improve the contact, in both n–i–p<sup>44</sup> and p–i–n architectures,<sup>45</sup> and there can be improved performance in devices with evaporated C<sub>60</sub> as opposed to solution-processed PCBM.<sup>46</sup>

The inhomogeneous region in the spiro-OMeTAD map stretches over 3 mm in length, suggesting that it may be prone to poor electronic contact over large length scales. Half-stacks with the bottom contacting layers look comparatively uniform, with the histograms largely resembling the shape of the reference used in each case. Looking at the images, however, we can see samples such as NiO<sub>x</sub> appear to have more spatial variation over their surface, despite having similar widths in the binned graphs.

We can quantify the inhomogeneity in the images by defining

$$\text{inhomogeneity ratio} = \frac{\frac{\text{IQR}}{\langle \text{QFLS} \rangle}}{\frac{\text{IQR}_{\text{ref}}}{\langle \text{QFLS}_{\text{ref}} \rangle}} \quad (13)$$

where IQR is the inter quartile range of the QFLS distribution in a map. This metric can be used to quantify the additional inhomogeneity in QFLS introduced when a transport layer is processed, while accounting for the varying mean QFLS found in different samples.

Comparing the inhomogeneity introduced by different transport layers (Figure 5a), we see that the bottom-contacting layers are fairly benign (inhomogeneity ratio ~1), while the top-contacting layers, particularly spiro-OMeTAD, are responsible for significantly more heterogeneity. This contrasting behavior could be a key determinant that confers upon the n–i–p and p–i–n structures their distinctive advantages and limitations and merits more detailed investigation.

The presented QFLS histograms encode information about the statistical distribution, but they say nothing about the length scales over which the variation occurs. In order to quantify this, we looked at the Fourier transforms (FTs) of the QFLS maps. The FT of a 2D image produces an image of the real image's frequency spectrum, which contains information about the length scale of the changes. Higher intensity farther from the center (high-frequency regions) indicates a smaller length scale of change (i.e., sharper changes in QFLS over the sample area). If the length scale of heterogeneity is large (i.e., a relatively uniform device), the FT will have high intensities at the center of the image and two perpendicular lines along the axes forming "cross hairs" (see Figure 5b).

The frequency distributions of the TL images all show this same cross-hair feature but have an additional Gaussian-like distribution that extends further into higher frequencies. The

poly-TPD FT closely resembles a uniform device, indicating that the QFLS is relatively free of sharp spatial variations. In contrast, the PTAA FT extends farther into the higher-frequency region, revealing sharper spatial variations in QFLS, despite having a histogram width similar to that of poly-TPD. In summary, the FT of the acquired parameter maps encodes information about the length scale of variations and is complementary to the histogram, which encodes the statistical distribution of variations.

While these results cannot be generalized to all possible deposition process for these transport layers, the heterogeneity introduced by a certain transport layer and some deposition-specific process can be assessed. On the basis of the capabilities of this technique, we propose an optimization workflow for identifying and addressing inhomogeneities in a device, illustrated in Figure 5c. If a device shows losses, it may be imaged in the setup and spatially resolved maps of QFLS, collection efficiency, ideality factor, and series resistance (the last using existing methods<sup>13</sup>) may be produced. If a parameter shows significant inhomogeneity over the device, the fabrication parameters can be iteratively modified using a Bayesian optimization. The process may be repeated, with half-stacks being imaged in addition to complete device stacks, to identify the specific problematic layers. If the cells are fully homogeneous and losses still persist, alternative materials or chemistries, such as new surface treatments and alternative transport layers, should be attempted.

To summarize, the scale-up of perovskite PV to the module scale ( $\sim 2 \text{ m}^2$ ) while high efficiencies (>23%) are retained is the key to commercialization and terawatt-scale deployment. In order to visualize heterogeneities over entire cell areas, we utilize a fast and relatively simple luminescence imaging method to produce maps of device-relevant parameters.

Our imaging reveals that perovskite cells exhibit significant spatial heterogeneities in V<sub>OC</sub> and charge collection at the 0.1–1 mm length scale. We experimentally demonstrate that the ratio of PLQEs at short circuit and open circuit can serve as an excellent indicator of current loss in perovskite solar cells. This enables us to visualize J<sub>SC</sub> loss over the active area, providing a very useful complement to established V<sub>OC</sub> mapping methods.

While inhomogeneities in the active layer have been imaged before, the effect of processing steps and transport layers has not been greatly investigated. We quantified the heterogeneity introduced when seven widely used transport layers are processed, thereby ranking them by suitability for upscaling. We find that top-contacting transport layers are the dominant source of heterogeneity in the stack. For instance, spiro-OMeTAD causes a 4-fold increase in heterogeneity when it is processed. In contrast, bottom-contacting layers are found to be relatively benign. This contrasting behavior could be a key determinant that confers upon the n–i–p and p–i–n structures their distinctive advantages and limitations and merits further investigation.

In comparison to slow (approximately hours) traditional mapping methods such as LBIC, luminescence imaging is fast (approximately minutes) and generates large amounts of data. By using such data gathered on a single device, we were able to validate the relationship between the ideality factor and QFLS. We believe that our relatively simple technique will be easy to implement for many scientists and development engineers, to use in combination with process development and high-throughput experimentation, in order to accelerate both laboratory research and industrial scale-up.

## ■ ASSOCIATED CONTENT

### § Supporting Information

The Supporting Information is available free of charge at <https://pubs.acs.org/doi/10.1021/acsenergylett.2c01094>.

Sample fabrication processes, detailed setup and measurement procedure, note on the Wong–Green formalism, note on the theory of luminescent imaging, illumination profile of the setup, spectral response of the setup, note on calculating PLQE maps using a white reference, JV curves of the main cells mapped, JV parameters of the main cells mapped, note on the effect of series and shunt resistance on  $Q_{col}$ , note on the error in  $Q_{col}$  maps due to uniform, unity ideality factor assumption, linearity of camera response, spectrum of the illumination source, error in PLQE maps due to optical losses not accounted for, validation of electronics of setup through JV measurement, example of an ideality factor calculation from the averaged value, and PLQE maps at open and short circuit of all cells used in the  $Q_{col}$  static plot ([PDF](#))

## ■ AUTHOR INFORMATION

### Corresponding Authors

**Suhas Mahesh** — Department of Physics, University of Oxford, Oxford OX1 3PU, U.K.; Edward S. Rogers Sr. Department of Electrical & Computer Engineering, University of Toronto, Toronto, Ontario M5S 3G8, Canada;  [orcid.org/0000-0002-3897-7963](https://orcid.org/0000-0002-3897-7963); Email: [suhas.mahesh@physics.ox.ac.uk](mailto:suhas.mahesh@physics.ox.ac.uk)

**Henry J. Snaith** — Department of Physics, University of Oxford, Oxford OX1 3PU, U.K.;  [orcid.org/0000-0001-8511-790X](https://orcid.org/0000-0001-8511-790X); Email: [henry.snaith@physics.ox.ac.uk](mailto:henry.snaith@physics.ox.ac.uk)

### Authors

**Akash Dasgupta** — Department of Physics, University of Oxford, Oxford OX1 3PU, U.K.;  [orcid.org/0000-0002-7942-293X](https://orcid.org/0000-0002-7942-293X)

**Pietro Caprioglio** — Department of Physics, University of Oxford, Oxford OX1 3PU, U.K.;  [orcid.org/0000-0002-3465-2475](https://orcid.org/0000-0002-3465-2475)

**Yen-Hung Lin** — Department of Physics, University of Oxford, Oxford OX1 3PU, U.K.;  [orcid.org/0000-0001-6819-1235](https://orcid.org/0000-0001-6819-1235)

**Karl-Augustin Zaininger** — Department of Physics, University of Oxford, Oxford OX1 3PU, U.K.

**Robert D.J. Oliver** — Department of Physics, University of Oxford, Oxford OX1 3PU, U.K.;  [orcid.org/0000-0003-4980-7940](https://orcid.org/0000-0003-4980-7940)

**Philippe Holzhey** — Department of Physics, University of Oxford, Oxford OX1 3PU, U.K.;  [orcid.org/0000-0003-3688-1607](https://orcid.org/0000-0003-3688-1607)

**Suer Zhou** — Department of Physics, University of Oxford, Oxford OX1 3PU, U.K.

**Melissa M. McCarthy** — Department of Physics, University of Oxford, Oxford OX1 3PU, U.K.;  [orcid.org/0000-0003-1512-2046](https://orcid.org/0000-0003-1512-2046)

**Joel A. Smith** — Department of Physics, University of Oxford, Oxford OX1 3PU, U.K.;  [orcid.org/0000-0001-6889-4408](https://orcid.org/0000-0001-6889-4408)

**Maximilian Frenzel** — Department of Physics, University of Oxford, Oxford OX1 3PU, U.K.; Department of Physical Chemistry, Fritz Haber Institute, 14195 Berlin, Germany

**M. Greyson Christoforo** — Department of Physics, University of Oxford, Oxford OX1 3PU, U.K.

**James M. Ball** — Department of Physics, University of Oxford, Oxford OX1 3PU, U.K.;  [orcid.org/0000-0003-1730-5217](https://orcid.org/0000-0003-1730-5217)

**Bernard Wenger** — Department of Physics, University of Oxford, Oxford OX1 3PU, U.K.;  [orcid.org/0000-0001-9026-7064](https://orcid.org/0000-0001-9026-7064)

Complete contact information is available at:  
<https://pubs.acs.org/10.1021/acsenergylett.2c01094>

### Author Contributions

¶A.D. and S.M. contributed equally.

### Notes

The authors declare the following competing financial interest(s): H.J.S. is a cofounder and CSO of Oxford PV Ltd.

## ■ ACKNOWLEDGMENTS

This work was part funded by the EPSRC, UK, under grant number EP/S00497/1 and the UKRI Global Challenge Research Fund project EP/P032591/1. A.D. and R.D.J.O. to express their gratitude to the Penrose scholarship for very generously funding their studentships. S.M. acknowledges the support of the Rhodes Scholarship and the Schmidt Science Fellowship. The research leading to these results has also received funding from the European Union's Horizon 2020 research and innovation programme MAESTRO under the Marie Skłodowska-Curie grant agreement No. 764787. The perceptually uniform color maps used in this work were kindly developed under the MIT licence by Fabio Crameri.<sup>47</sup> Emoji artwork used in Figure 5 was taken from the “Google Noto font” suite,<sup>48</sup> which is provided as free and open source under the Apache license, version 2.0.

## ■ REFERENCES

- (1) Haegel, B. N. M.; Margolis, R.; Buonassisi, T.; Feldman, D.; Garabedian, R.; Green, M.; Glunz, S.; Henning, H.; Holder, B.; Kaizuka, I.; Kroposki, B.; Matsubara, K.; Niki, S.; Sakurai, K.; Schindler, R. A.; Tumas, W.; Weber, E. R.; Wilson, G.; Woodhouse, M.; Kurtz, S.; Haegel, N. M.; Margolis, R.; Buonassisi, T.; Feldman, D.; Froitzheim, A.; Garabedian, R.; Green, M.; Glunz, S.; Henning, H.; Holder, B.; Kaizuka, I.; Kroposki, B.; Matsubara, K.; Niki, S.; Sakurai, K.; Schindler, R. A.; Tumas, W.; Weber, E. R.; Wilson, G.; Woodhouse, M.; Kurtz, S. Terawatt-Scale Photovoltaics: Trajectories and Challenges. *Science* (1979) **2017**, 356 (6334), 141–143.
- (2) Best Research-Cell Efficiency Chart; <https://www.nrel.gov/pv/cell-efficiency.html> (accessed 2021-10-27).
- (3) Yablonovitch, E.; Miller, O. D.; Miller, O. D.; Miller, O. D. The Opto-Electronics Which Broke the Efficiency Record in Solar Cells. Conference on Lasers and Electro-Optics 2012; 2012; paper CF2J.1.
- (4) Rau, U. Reciprocity Relation between Photovoltaic Quantum Efficiency and Electroluminescent Emission of Solar Cells. *Physical Review B - Condensed Matter and Materials Physics* **2007**, 76 (8), 085303.
- (5) Kirchartz, T.; Márquez, J. A.; Stolterfoht, M.; Unold, T. Photoluminescence-Based Characterization of Halide Perovskites for Photovoltaics. *Adv. Energy Mater.* **2020**, 10 (26), 1904134.
- (6) Peter Würfel, U. W. *Physics of Solar Cells: Basic Principles to Advanced Concepts*, 3rd ed.; Wiley: 2016; p 288.
- (7) Tennyson, E. M.; Doherty, T. A. S.; Stranks, S. D. Heterogeneity at Multiple Length Scales in Halide Perovskite Semiconductors. *Nature Reviews Materials* **2019** 4:9 **2019**, 4 (9), 573–587.
- (8) Frohmaier, K.; Anaya, M.; Macpherson, S.; Sung, J.; Doherty, T. A. S.; Chiang, Y.-H.; Winchester, A. J.; Orr, K. W. P.; Parker, J. E.; Quinn, P. D.; Dani, K. M.; Rao, A.; Stranks, S. D. Nanoscale Chemical

- Heterogeneity Dominates the Optoelectronic Response of Alloyed Perovskite Solar Cells. *Nature Nanotechnology* **2022**, *17* (2), 190–196.
- (9) Stolterfoht, M.; Wolff, C. M.; Márquez, J. A.; Zhang, S.; Hages, C. J.; Rothhardt, D.; Albrecht, S.; Burn, P. L.; Meredith, P.; Unold, T.; Neher, D. Visualization and Suppression of Interfacial Recombination for High-Efficiency Large-Area Pin Perovskite Solar Cells. *Nature Energy* **2018**, *3* (10), 847–854.
- (10) Padilla, M.; Michl, B.; Thaidigsmann, B.; Warta, W.; Schubert, M. C. Short-Circuit Current Density Mapping for Solar Cells. *Sol. Energy Mater. Sol. Cells* **2014**, *120*, 282–288.
- (11) Mundt, L. E.; Kwapil, W.; Yakoob, M. A.; Herterich, J. P.; Kohlstadt, M.; Wurfel, U.; Schubert, M. C.; Glunz, S. W. Quantitative Local Loss Analysis of Blade-Coated Perovskite Solar Cells. *IEEE Journal of Photovoltaics* **2019**, *9* (2), 452–459.
- (12) Kampwerth, H.; Trupke, T.; Weber, J. W.; Augarten, Y. Advanced Luminescence Based Effective Series Resistance Imaging of Silicon Solar Cells. *Appl. Phys. Lett.* **2008**, *93* (20), 202102.
- (13) Trupke, T.; Pink, E.; Bards, R. A.; Abbott, M. D. Spatially Resolved Series Resistance of Silicon Solar Cells Obtained from Luminescence Imaging. *Appl. Phys. Lett.* **2007**, *90* (9), 093506.
- (14) Würfel, P.; Trupke, T.; Puzzer, T.; Schäffer, E.; Warta, W.; Glunz, S. W. Diffusion Lengths of Silicon Solar Cells from Luminescence Images. *J. Appl. Phys.* **2007**, *101* (12), 123110.
- (15) Fuyuki, T.; Kondo, H.; Yamazaki, T.; Takahashi, Y.; Uraoka, Y. Photographic Surveying of Minority Carrier Diffusion Length in Polycrystalline Silicon Solar Cells by Electroluminescence. *Appl. Phys. Lett.* **2005**, *86* (26), 262108.
- (16) Draguta, S.; Christians, J. A.; Morozov, Y. v.; Mucunzi, A.; Manser, J. S.; Kamat, P. v.; Luther, J. M.; Kuno, M. A Quantitative and Spatially Resolved Analysis of the Performance-Bottleneck in High Efficiency, Planar Hybrid Perovskite Solar Cells †. *Energy Environ. Sci.* **2018**, *11*, 960.
- (17) Mastroianni, S.; Heinz, F. D.; Im, J.-H.; Veurman, W.; Padilla, M.; Schubert, M. C.; Würfel, U.; Grätzel, M.; Park, N.-G.; Hinsch, A. Analysing the Effect of Crystal Size and Structure in Highly Efficient  $\text{CH}_3\text{NH}_3\text{PbI}_3$  Perovskite Solar Cells by Spatially Resolved Photo- and Electroluminescence Imaging. *Nanoscale* **2015**, *7* (46), 19653–19662.
- (18) Okano, M.; Endo, M.; Wakamiya, A.; Yoshita, M.; Akiyama, H.; Kanemitsu, Y. Degradation Mechanism of Perovskite  $\text{CH}_3\text{NH}_3\text{PbI}_3$  Diode Devices Studied by Electroluminescence and Photoluminescence Imaging Spectroscopy. *Applied Physics Express* **2015**, *8* (10), 102302.
- (19) Soufiani, A. M.; Tayebjee, M. J. Y.; Meyer, S.; Ho-Baillie, A.; Sung Yun, J.; MacQueen, R. W.; Spiccia, L.; Green, M. A.; Hameiri, Z. Electro- and Photoluminescence Imaging as Fast Screening Technique of the Layer Uniformity and Device Degradation in Planar Perovskite Solar Cells. *J. Appl. Phys.* **2016**, *120* (3), 035702.
- (20) Schubert, M. C.; Mundt, L. E.; Walter, D.; Fell, A.; Glunz, S. W. Spatially Resolved Performance Analysis for Perovskite Solar Cells. *Adv. Energy Mater.* **2020**, *10* (26), 1904001.
- (21) Bui, A. D.; Mozaffari, N.; Truong, T. N.; Duong, T.; Weber, K. J.; White, T. P.; Catchpole, K. R.; Macdonald, D.; Nguyen, H. T. Electrical Properties of Perovskite Solar Cells by Illumination Intensity and Temperature-dependent Photoluminescence Imaging. *Progress in Photovoltaics: Research and Applications* **2021**, DOI: 10.1002/pip.3498.
- (22) Rau, U.; Kirchartz, T. The Principle of Detailed Balance and the Opto-Electronic Properties of Solar Cells. In *Photon Management in Solar Cells*; Wiley: 2015; pp 21–48.
- (23) Wong, J.; Green, M. A. From Junction to Terminal: Extended Reciprocity Relations in Solar Cell Operation. *Physical Review B - Condensed Matter and Materials Physics* **2012**, *85* (23), 235205.
- (24) Rau, U.; Huhn, V.; Stoicescu, L.; Schneemann, M.; Augarten, Y.; Gerber, A.; Pieters, B. E. Photocurrent Collection Efficiency Mapping of a Silicon Solar Cell by a Differential Luminescence Imaging Technique. *Appl. Phys. Lett.* **2014**, *105* (16), 163507.
- (25) El-Hajje, G.; Momblona, C.; Gil-Escríg, L.; Avila, J.; Guillemot, T.; Guillemoles, J. F.; Sessolo, M.; Bolink, H. J.; Lombez, L. Quantification of Spatial Inhomogeneity in Perovskite Solar Cells by Hyperspectral Luminescence Imaging. *Energy Environ. Sci.* **2016**, *9* (7), 2286–2294.
- (26) Ren, A.; Lai, H.; Hao, X.; Tang, Z.; Xu, H.; Yu Jeco, B. M. F.; Watanabe, K.; Wu, L.; Zhang, J.; Sugiyama, M.; Wu, J.; Zhao, D. Efficient Perovskite Solar Modules with Minimized Nonradiative Recombination and Local Carrier Transport Losses. *Joule* **2020**, *4* (6), 1263–1277.
- (27) Stolterfoht, M.; le Corre, V. M.; Feuerstein, M.; Caprioglio, P.; Koster, L. J. A.; Neher, D. Voltage-Dependent Photoluminescence and How It Correlates with the Fill Factor and Open-Circuit Voltage in Perovskite Solar Cells. *ACS Energy Letters* **2019**, *4* (12), 2887–2892.
- (28) Thiesbrummel, J.; le Corre, V. M.; Peña-Camargo, F.; Perdigón-Toro, L.; Lang, F.; Yang, F.; Grischek, M.; Gutierrez-Partida, E.; Warby, J.; Farrar, M. D.; Mahesh, S.; Caprioglio, P.; Albrecht, S.; Neher, D.; Snaith, H. J.; Stolterfoht, M. Universal Current Losses in Perovskite Solar Cells Due to Mobile Ions. *Adv. Energy Mater.* **2021**, *11* (34), 2101447.
- (29) Du, T.; Xu, W.; Xu, S.; Ratnasingham, S. R.; Lin, C. T.; Kim, J.; Briscoe, J.; McLachlan, M. A.; Durrant, J. R. Light-Intensity and Thickness Dependent Efficiency of Planar Perovskite Solar Cells: Charge Recombination versus Extraction. *Journal of Materials Chemistry C* **2020**, *8* (36), 12648–12655.
- (30) Caprioglio, P.; Stolterfoht, M.; Wolff, C. M.; Unold, T.; Rech, B.; Albrecht, S.; Neher, D. On the Relation between the Open-Circuit Voltage and Quasi-Fermi Level Splitting in Efficient Perovskite Solar Cells. *Adv. Energy Mater.* **2019**, *9* (33), 1901631.
- (31) Caprioglio, P.; Wolff, C. M.; Sandberg, O. J.; Armin, A.; Rech, B.; Albrecht, S.; Neher, D.; Stolterfoht, M. On the Origin of the Ideality Factor in Perovskite Solar Cells. *Adv. Energy Mater.* **2020**, *10* (27), 2000502.
- (32) Sarritzu, V.; Sestu, N.; Marongiu, D.; Chang, X.; Masi, S.; Rizzo, A.; Colella, S.; Quochi, F.; Saba, M.; Mura, A.; Bongiovanni, G. Optical Determination of Shockley-Read-Hall and Interface Recombination Currents in Hybrid Perovskites. *Sci. Rep.* **2017**, *7* (1), 44629.
- (33) Hameiri, Z.; Chaturvedi, P.; McIntosh, K. R. Imaging the Local Ideality Factor by Contactless Photoluminescence Measurement. *Appl. Phys. Lett.* **2013**, *103* (2), 023501.
- (34) Onno, A.; Chen, C.; Koswatta, P.; Boccard, M.; Holman, Z. C. Passivation, Conductivity, and Selectivity in Solar Cell Contacts: Concepts and Simulations Based on a Unified Partial-Resistances Framework. *J. Appl. Phys.* **2019**, *126*, 183103.
- (35) Tvingstedt, K.; Malinkiewicz, O.; Baumann, A.; Deibel, C.; Snaith, H. J.; Dyakonov, V.; Bolink, H. J. Radiative Efficiency of Lead Iodide Based Perovskite Solar Cells. *Scientific Reports* **2014**, *4* (1), 1–7.
- (36) Würfel, P. The Chemical Potential of Radiation. *J. Phys. C: Solid State Phys.* **1982**, *15*, 3967–3985.
- (37) Hall, R. N. Electron-Hole Recombination in Germanium. *Phys. Rev.* **1952**, *87* (2), 387.
- (38) Shockley, W.; Read, W. T. Statistics of the Recombinations of Holes and Electrons. *Phys. Rev.* **1952**, *87* (5), 835.
- (39) Courtier, N. E. Interpreting Ideality Factors for Planar Perovskite Solar Cells: Ecotypal Diode Theory for Steady-State Operation. *Physical Review Applied* **2020**, *14* (2), 024031.
- (40) ANDOR (Oxford instruments). *Zyla SCmos: Manufacturer Specification Sheet*.
- (41) Kerr, M. J.; Cuevas, A.; Sinton, R. A. Generalized Analysis of Quasi-Steady-State and Transient Decay Open Circuit Voltage Measurements. *J. Appl. Phys.* **2002**, *91* (1), 399.
- (42) Hinken, D.; Bothe, K.; Ramspeck, K.; Herlufsen, S.; Brendel, R. Determination of the Effective Diffusion Length of Silicon Solar Cells from Photoluminescence. *J. Appl. Phys.* **2009**, *105* (10), 104516.
- (43) Rau, U.; Huhn, V.; Pieters, B. E. Luminescence Analysis of Charge-Carrier Separation and Internal Series-Resistance Losses in Cu (In,Ga)Se<sub>2</sub> Solar Cells. *Physical Review Applied* **2020**, *14* (1), 014046.

- (44) McCarthy, M. M.; Walter, A.; Moon, S. J.; Noel, N. K.; O'Brien, S.; Pemble, M. E.; Nicolay, S.; Wenger, B.; Snaith, H. J.; Povey, I. M. Atomic Layer Deposited Electron Transport Layers in Efficient Organometallic Halide Perovskite Devices. *MRS Advances* **2018**, 3 (S1), 3075–3084.
- (45) Zhu, Z.; Bai, Y.; Liu, X.; Chueh, C. C.; Yang, S.; Jen, A. K. Y. Enhanced Efficiency and Stability of Inverted Perovskite Solar Cells Using Highly Crystalline SnO<sub>2</sub> Nanocrystals as the Robust Electron-Transporting Layer. *Adv. Mater.* **2016**, 28 (30), 6478–6484.
- (46) Liu, X.; Liu, Z.; Ye, H.; Tu, Y.; Sun, B.; Tan, X.; Shi, T.; Tang, Z.; Liao, G. Novel Efficient C60-Based Inverted Perovskite Solar Cells with Negligible Hysteresis. *Electrochim. Acta* **2018**, 288, 115–125.
- (47) Crameri, F. Scientific Colour Maps; Zenodo2021; <https://zenodo.org/record/5501399>
- (48) Google LLC. *Noto Emoji fonts* <https://github.com/googlefonts/noto-emoji> (accessed 2021-11-22).

## □ Recommended by ACS

---

### Perovskite Carrier Transport: Disentangling the Impacts of Effective Mass and Scattering Time Through Microscopic Optical Detection

Andrew H. Hill, Erik M. Grumstrup, *et al.*

MAY 11, 2018

THE JOURNAL OF PHYSICAL CHEMISTRY LETTERS

READ ▶

---

### Nanoscale-Resolved Surface-to-Bulk Electron Transport in CsPbBr<sub>3</sub> Perovskite

Serhii Polishchuk, Majed Chergui, *et al.*

JANUARY 19, 2022

NANO LETTERS

READ ▶

---

### Spatial Distribution of Solar Cell Parameters in Multigrain Halide-Perovskite Films: A Device Model Perspective

Sapir Bitton, Nir Tessler, *et al.*

SEPTEMBER 03, 2021

ACS APPLIED ENERGY MATERIALS

READ ▶

---

### Degradation of Perovskite Photovoltaics Manifested in the Cross-Sectional Potential Profile Studied by Quantitative Kelvin Probe Force Microscopy

Maki Hiraoka, Yasuhiro Shirai, *et al.*

APRIL 08, 2022

ACS APPLIED ENERGY MATERIALS

READ ▶

[Get More Suggestions >](#)